Chen *et al. Advances in Aerodynamics* (2023) 5:12
https://doi.org/10.1186/s42774-023-00147-z

Advances in Aerodynamics

RESEARCH Open Access

Constrained large-eddy simulation of laminar-turbulent transition in compressible channel flows

Sanmu Chen[1,2], Zhou Jiang[3], Minping Wan[1,2*] and Shiyi Chen[1,2]

*Correspondence:
wanmp@sustech.edu.cn

[1] Guangdong Provincial Key Laboratory of Turbulence Research and Applications, Department of Mechanics and Aerospace Engineering, Southern University of Science and Technology, Shenzhen 518055, China
[2] Guangdong-Hong Kong-Macao Joint Laboratory for Data-Driven Fluid Mechanics and Engineering Applications, Southern University of Science and Technology, Shenzhen 518055, China
[3] College of Aerospace Engineering, Chongqing University, Chongqing 400044, China

Abstract

An improved approach for constrained large-eddy simulations (CLES) of wall-bounded compressible transitional flows is proposed by introducing an intermittency factor. The improved model is tested and validated with compressible channel flows at various Mach numbers and Reynolds numbers that are transitioning from laminar to turbulent states. The improved model is compared against traditional dynamic Smagorinsky model (DSM) and Direct Numerical Simulations (DNS), where the improved model is in better agreement with DNS results than traditional DSM model, in terms of mean velocity profiles, total Reynolds stress and total heat flux. Therefore, the proposed method can be used to accurately predict the temporal laminar-turbulent transition process of compressible wall-bounded flows.

Keywords: Constrained LES, Transition prediction, Compressible channel flow

1 Introduction

Accurate evaluation of the laminar-turbulent transition in compressible wall bounded flows is critical to the advancement of supersonic and hypersonic aircraft design. There is a significant difference between laminar and turbulent flows [1], for instance, the friction and heat flux under turbulent state can be 3 to 5 times higher than in laminar flows [2]. Considerable efforts have been placed in understanding the physical mechanisms of the laminar turbulent transition using Direct Numerical Simulations (DNS) over the past years to improve the prediction of the onset of transition in large-eddy simulations (LES) and Reynolds-averaged Navier-Stokes (RANS) methods [1, 3].

DNS method resolves all relevant length scales without invoking any turbulence models, making it the most suitable approach to further our understanding on the transition process. Orszag and Kells [4] utilized DNS to investigate the effects of Reynolds number on the transition process in two difference incompressible configurations with finite amplitude disturbance: (i) plane Poiseuille flow and (ii) plane Couette flow. Subsequently, Sayadi, Hamman, and Moin [5] studied the H- and K- type of transition process and found that there is a correlation between the location of maximum skin-friction and the onset of self-sustaining mechanism in near wall turbulence DNS. Zhao and Yang

[6] investigated the relationship between vortex reconnection and the sharp increase of skin-friction in the K-type temporal transition in a channel flow, where they found that the surge of skin-friction coefficient occurs at the identified reconnection time. This is due to the rapid reconnection of vortex lines that could induce a velocity that is opposite to the mean flow, accelerating the near-wall fluid motion in the flow with constant mass flux. While the DNS is a powerful tool to further our understanding on the transition mechanism, its usefulness in engineering applications is hindered by the extensive requirements in numerical grid points and computational power.

In contrary to DNS, the LES resolves only the large-scale eddies, while relying on the sub-grid stress (SGS) model to accurately predict the small scale. Hence, the grid resolution requirement for LES is significantly less than DNS, allowing LES, combined with proper wall models, to be used in large industrial applications. Nevertheless, since LES relies heavily on the SGS model to capture accurately the small scale, the accuracy of the LES method lies within the sub-grid scale model. Ducros, Comte and Lesieur [7] investigated the suitability of LES on predicting the laminar-turbulent transition process in a spatially developing turbulent boundary layer over a flat plate, where they found that LES could capture the linear growth of Tollmien-Schlichting (TS) waves and the secondary instability. Sayadi and Moin [8] assessed the performance of three different SGS models, namely, the dynamic Smagorinsky eddy viscosity model [9], dynamic scale similarity model [10], and dynamic one equation model based on the SGS kinetic energy [11], where they found these models underpredicted the overshoot in skin friction profile at the end of the laminar-turbulent transition. Most importantly, the deviation from DNS results increases as the grid resolution gets coarser. Recently, an SGS eddy viscosity model that is based on the relations of eddy-viscosity and the product of the large-scale velocity strain-rate tensor with the symmetric part of the large-scale vorticity gradient [12, 13] is proposed to tackle the laminar turbulent transition process. The theoretical analysis showed that the model is capable of distinguishing between laminar and turbulent states. In addition, their simulation results further demonstrated the capability of the model to predict accurately the onset of transition, friction peak, mean velocity profile, mean temperature profile and turbulence intensities. However, the large grid requirements in the near-wall region for these models to accurately predict the laminar-turbulent transition process have hindered its usefulness for practical industrial problems [14].

RANS method is still a popular choice across all types of industrial applications due to its high efficiency and satisfactory accuracy, especially after the introduction of the local-correction-based transition $\gamma - Re_\theta$ model by Menter and Langtry et al. [15–17]. The main advantage of the model is that it uses experimental data to associate the transition momentum thickness Reynolds number with physical parameters such as local turbulence intensity and pressure gradient, where the transition criterion is determined by the ratio of local vorticity Reynolds number and critical momentum thickness Reynolds number. Hence, the transition model is compatible with modern CFD approaches, i.e., unstructured grids and massive parallel execution. However, the model has no physical mechanism of the transition process and it is rather an ad-hoc model determined through brute force. The $\gamma - Re_\theta$ model has successfully been mainly used in the simulation of low-speed boundary layer transition

flow with further improvement done to the model by Krause, Behr and Ballmann [18] for hypersonic boundary layer transition simulations. Krause, Behr and Ballmann [18] constructed a relationship between F_{length} and $Re_{\theta c}$ by considering freestream turbulence intensities, allowing the simulation results to agree well with the experimental data in the cases of hypersonic double ramp. Bensassi, Lani and Rambaud [19] tested the model by simulating a Mach 8 flow over a 7° half angle sharp cone at three different freestream turbulence intensity levels, where they reported that the heat flux in the transition regime shows excellent agreement with experimental data. Zhang et al. [20, 21] calibrated the basic $\gamma - Re_{\theta}$ empirical correlation with different samples and results in different cases are satisfactory.

Therefore, the couple of RANS and LES methods could combine the best of both worlds to achieve a good balance between computational efficiency and accuracy to capture important features of unsteady flows with large separations in large industrial applications [22–24]. The RANS-LES hybrid methods usually decompose the computational domain into inner and outer regions with the RANS method handling the inner region and the LES method resolving the outer region. Detached-eddy simulation (DES) is a representative of the RANS-LES hybrid method, which was first proposed in 1997 and has been widely used in wall turbulence at high Reynolds numbers [25]. Although the DES method has achieved great success in engineering flows, some non-physical problems such as log-layer mismatch (LLM) still exist in the wall turbulence. Delayed DES (DDES) [23] and improved delayed DES (IDDES) [26] are subsequently developed to address these issues by altering the formulation of the length-scale function, but these schemes introduced other non-physical factors.

The main reason for the existence of LLM is the obvious difference in the fluctuation information near the interface. Chen et al. [27] proposed a new method, namely the constrained large-eddy simulation (CLES), that simulates the whole flow domain by LES while enforcing a Reynolds stress constraint on the mean part of SGS model in the inner layer. It has been demonstrated to achieve remarkable results in the incompressible channel flow and the flow with separation. Jiang et al. [28] further extended the CLES method for compressible wall-bounded turbulence by decomposing the SGS stress and heat flux into their mean part and fluctuation part in the near-wall region, with the mean SGS stress and heat flux being constrained by the prescribed Reynolds stress model and turbulent heat flux model, respectively. Zhang et al. [29, 30] simulated a turbulent flow over rough walls in the framework of CLES by invoking the rough-wall-like mean shear model without actually resolving the roughness elements. The statistical results from the work of Zhang et al. [29, 30] show that the effect of rough-wall-like mean shear on the turbulent flow is similar to that of roughness elements and the approach based on CLES can be used as a new wall model for the simulation of the rough-wall flows. Zhao et al. [31] incorporated an intermittency factor into the CLES method, where their improved model is capable of predicting accurately the transition onset of laminar-turbulent transition in incompressible channel flow. However, their model is unable to capture the maximum skin friction at later stage of the transition. Wang et al. [32] introduced a transition-predictive RANS model as the controlling condition to the CLES (TrCLES). The TrCLES method performed excellent well in predicting the laminar separation bubble

and separation-induced transition process in both the Eppler 387 (E387) airfoil and the ultra-high-lift low-pressure turbine T106C flows.

In this paper, we extend Zhao et al.'s [31] method by constructing an intermittency factor with CLES that is capable of predicting the transition process in wall bounded compressible flows. In the next section, required mathematical background and the simulation parameters are provided. Numerical results obtained from DNS, DSM-based LES and CLES are presented in Section 3, followed by concluding remarks.

2 Problem formulation

2.1 Governing equations

The filtered conservation of mass, momentum, and energy equations in the context of LES employed in this study to describe the compressible flows are formulated as [33]:

$$\frac{\partial \bar{\rho}}{\partial t} + \frac{\partial(\bar{\rho}\tilde{u}_i)}{\partial x_i} = 0, \tag{1}$$

$$\frac{\partial(\bar{\rho}\tilde{u}_i)}{\partial t} + \frac{\partial\left(\bar{\rho}\tilde{u}_i\tilde{u}_j + \bar{p}\delta_{ij}\right)}{\partial x_j} = \frac{1}{Re}\frac{\partial\tilde{\sigma}_{ij}}{\partial x_j} + \frac{\partial\tau_{ij}^{LES}}{\partial x_j}, \tag{2}$$

$$\frac{\partial(\bar{\rho}\tilde{e})}{\partial t} + \frac{\partial[\tilde{u}_i(\bar{\rho}\tilde{e} + \bar{p})]}{\partial x_i} = \frac{\partial\tilde{q}_i}{\partial x_i} + \frac{\partial\left(\tilde{\sigma}_{ij}\tilde{u}_j\right)}{\partial x_i} + \frac{\partial q_i^{LES}}{\partial x_i} + \frac{\partial\left(\tau_{ij}^{LES}\tilde{u}_j\right)}{\partial x_i}, \tag{3}$$

where $\bar{\cdot}$ and $\tilde{\cdot}$ represent the spatial and Favre filter, respectively, with a filter width of $\bar{\Delta}$. The Favre averaging operation of a flow field variable $\mathcal{F}$ is defined as:

$$\widetilde{\mathcal{F}}(x_i, t) = \frac{\overline{\rho\mathcal{F}}}{\bar{\rho}}. \tag{4}$$

Here, $\bar{p} = \bar{\rho}R\widetilde{T}$ is the static pressure, $\bar{\rho}$ is the density, $\tilde{u}_i$ is the velocity vector, $\widetilde{T}$ is the temperature, R is the specific gas constant, $\tilde{e} = C_v\widetilde{T} + \frac{1}{2}\tilde{u}_i\tilde{u}_i$ is the total energy per unit mass, $C_v = 1/\left[\alpha(\alpha-1)M_\infty^2\right]$ is the specific heat at constant volume, $M_\infty = U_\infty/\sqrt{\alpha R T_\infty}$ is the Mach number, and α is the ratio of specific heat with a value of 1.4 adopted in this study. The viscous stress tensor $\tilde{\sigma}_{ij}$ is described as

$$\tilde{\sigma}_{ij} = \mu\left(\frac{\partial\tilde{u}_i}{\partial x_j} + \frac{\partial\tilde{u}_j}{\partial x_i}\right) - \frac{2}{3}\mu\frac{\partial\tilde{u}_k}{\partial x_k}\delta_{ij}, \tag{5}$$

and the heat flux vector $\tilde{q}_i$ is determined as

$$\tilde{q}_i = -\frac{C_p\mu}{Pr}\frac{\partial\widetilde{T}}{\partial x_i}, \tag{6}$$

where $C_p = \alpha C_v$ is the specific heat at constant pressure and Pr is the molecular Prandtl number. $Pr = 0.7$ is adopted in this study. The molecular viscosity is computed using Sutherland's law:

$$\mu = \widetilde{T}^{3/2}\frac{1+S}{\widetilde{T}+S}, \tag{7}$$

with $S = 110.3\,\mathrm{K}/T_\infty$. The unclosed terms in Eqs. (2) and (3) are the SGS stress tensor and the SGS heat flux vector, respectively, and they are given as:

$$\tau_{ij}^{LES} = -\bar{\rho}\left(\widetilde{u_i u_j} - \tilde{u}_i\tilde{u}_j\right), \tag{8}$$

$$q_i^{LES} = \bar{\rho}C_p\left(\widetilde{Tu_i} - \widetilde{T}\tilde{u}_i\right), \tag{9}$$

where the closures for the two terms are provided in the following section.

2.2 CLES

In the CLES method, the flow field is divided into near-wall inner region and outer region, and the governing equations introduced in Section 2.1 are numerically solved in both the inner and outer regions. In the outer region, the Smagorinsky model introduced by Yoshizawa [34] for compressible turbulence is employed in this study as follows:

$$\tau_{ij}^{SGS} = 2C_S^2\bar{\rho}\bar{\Delta}^2\|\tilde{S}\|\left(\tilde{S}_{ij} - \frac{1}{3}\tilde{S}_{kk}\delta_{ij}\right) - \frac{2}{3}C_I\bar{\rho}\bar{\Delta}^2\|\tilde{S}\|^2\delta_{ij}, \tag{10}$$

$$q_i^{SGS} = -C_S^2\frac{\bar{\Delta}^2\bar{\rho}C_p\|\tilde{S}\|}{Pr_T}\frac{\partial\widetilde{T}}{\partial x_j}, \tag{11}$$

where $\bar{\Delta}$ is the grid scale and $\|\tilde{S}\| = \left(2\tilde{S}_{ij}\tilde{S}_{ij}\right)^{1/2}$ is the magnitude of $\tilde{S}_{ij}$. The constants, C_S, C_I and Pr_T, in the above equations are computed dynamically following ref. [35]. The boundary separating both constrained and non-constrained regions is determined automatically using the DES criterion [25, 28].

On the other hand, the τ_{ij}^{LES} and heat flux q_i^{LES} in the near-wall region are split into the mean and fluctuating parts as [28]:

$$\tau_{ij}^{LES} = \left\langle\tau_{ij}^{LES}\right\rangle + \left(\tau_{ij}^{LES}\right)' \tag{12}$$

and

$$q_i^{LES} = \left\langle q_i^{LES}\right\rangle + \left(q_i^{LES}\right)', \tag{13}$$

respectively, where $\langle\cdot\rangle$ represents ensemble averaging over the statistically homogeneous direction. The density weighted Reynolds averaging (also referred to as Favre averaging) is defined as:

$$\{\mathcal{F}\} = \frac{\langle\rho\mathcal{F}\rangle}{\langle\rho\rangle}. \tag{14}$$

The mean SGS stress and heat flux are constrained by Reynolds stress and heat flux approximately by RANS models through the following relations:

$$\left\langle \tau_{ij}^{LES} \right\rangle = \tau_{ij}^{RANS} + \langle \bar{\rho} \rangle \left(\{ \tilde{u}_i \tilde{u}_j \} - \{ \tilde{u}_i \} \{ \tilde{u}_j \} \right) \tag{15}$$

and

$$\left\langle q_i^{LES} \right\rangle = q_i^{RANS} - C_p \langle \bar{\rho} \rangle \left(\left\{ \tilde{u}_i \widetilde{T} \right\} - \{ \tilde{u}_i \} \left\{ \widetilde{T} \right\} \right). \tag{16}$$

Here,$-\langle \bar{\rho} \rangle \left(\{ \tilde{u}_i \tilde{u}_j \} - \{ \tilde{u}_i \} \{ \tilde{u}_j \} \right)$ and $\langle \bar{\rho} \rangle C_p \left(\left\{ \tilde{u}_i \widetilde{T} \right\} - \{ \tilde{u}_i \} \left\{ \widetilde{T} \right\} \right)$ are the resolved Reynolds stress and heat flux respectively. The expressions of τ_{ij}^{RANS} and q_i^{RANS} can be obtained from the governing equations of RANS [28]:

$$\tau_{ij}^{RANS} = -\langle \rho \rangle \left(\{ u_i u_j \} - \{ u_i \} \{ u_j \} \right) \tag{17}$$

and

$$q_i^{RANS} = \langle \rho \rangle C_p (\{ u_i T \} - \{ u_i \} \{ T \}). \tag{18}$$

τ_{ij}^{RANS} and q_i^{RANS} can be modeled from different models for the specific flow geometry, such as $k - \epsilon$ model, $k - \omega$ model [36], Baldwin-Lomax (B-L) model [37], SST model [38], etc. In the present work, the turbulent viscosity μ_t is calculated from the one equation Spalart-Allmaras (S-A) model [39].

The fluctuation parts of the SGS stress tensor and heat flux vector are given by

$$\left(\tau_{ij}^{LES} \right)' = \tau_{ij}^{SGS} - \left\langle \tau_{ij}^{SGS} \right\rangle, \tag{19}$$

$$\left(q_i^{LES} \right)' = q_i^{SGS} - \left\langle q_i^{SGS} \right\rangle, \tag{20}$$

where τ_{ij}^{SGS} and q_i^{SGS} are calculated from traditional SGS stress and heat flux vector in LES. Hence, the full expression of the SGS stress tensor and heat flux vector in near-wall regions reads:

$$\tau_{ij}^{LES} = \tau_{ij}^{RANS} + \langle \bar{\rho} \rangle \left(\{ \tilde{u}_i \tilde{u}_j \} - \{ \tilde{u}_i \} \{ \tilde{u}_j \} \right) + \left(\tau_{ij}^{SGS} - \left\langle \tau_{ij}^{SGS} \right\rangle \right), \tag{21}$$

$$q_i^{LES} = q_i^{RANS} - C_p \langle \bar{\rho} \rangle \left(\left\{ \tilde{u}_i \widetilde{T} \right\} - \{ \tilde{u}_i \} \left\{ \widetilde{T} \right\} \right) + \left(q_i^{SGS} - \left\langle q_i^{SGS} \right\rangle \right). \tag{22}$$

2.3 Intermittency factor

The original unmodified CLES method has been demonstrated by Zhao et al. [31] to be unable to capture the transition process accurately. Hence, they introduced an intermittency factor to the CLES method to improve its predictability in an incompressible channel transition problem. Intermittency factor is widely used in RANS models and we have included it in the theoretical framework of CLES, allowing us to select any available transitional RANS model as a constraint within the CLES method for transitional flows. In the present work, the intermittency factor based on the one equation S-A eddy

viscosity model is selected due to its simplicity and without introducing any additional extra equations.

The turbulent eddy-viscosity μ_t used in the Reynolds stress constraint in the CLES of transitional flows can be reformulated by introducing an intermittency factor γ such that $\mu_t^{\gamma} = \gamma \mu_t$. Following the works of Piomelli et al. [40] and Zhao et al. [31], we extend the intermittency factor γ to be used in compressible transitional flows.

$$\gamma = \frac{H_l - H_{12}}{H_l - H_t}. \tag{23}$$

Here, H_l and H_t are the shape factors of laminar and turbulent channel flows, respectively. In this present study, H_t is fixed at approximately 1.7 and H_l varies from 2.2 to 2.7, respectively. H_{12} is the shape factor and its value varies within the transition layer as:

$$H_{12} = \frac{\delta_1(x)}{\delta_2(x)}, \tag{24}$$

where $\delta_1(x)$ and $\delta_2(x)$ are the displacement thickness and momentum thickness, respectively [41]:

$$\delta_1(x) = \int_0^{H/2} \left(1 - \frac{\rho u}{\rho_\infty U_\infty}\right) dy, \tag{25}$$

$$\delta_2(x) = \int_0^{H/2} \frac{\rho u}{\rho_\infty U_\infty} \left(1 - \frac{u}{U_\infty}\right) dy, \tag{26}$$

with ρ_∞ and U_∞ being the density and speed of the free-stream, respectively.

2.4 Test cases

The suitability and performance of the CLES method for transitional flows are evaluated on three-dimensional compressible channel flows with temporal mode at different Mach numbers and Reynolds numbers. The simulation results obtained from the CLES method are compared to conventional DNS and DSM-based LES methods in three cases with $M_\infty = 1.5$ and $Re_\infty = 3000$, $M_\infty = 2.0$ and $Re_\infty = 3500$, $M_\infty = 3.0$ and $Re_\infty = 4880$, respectively. The LES based on the dynamic Smagorinsky model (DSM) will be referred hereafter as LES. All three methods have identical simulation setup and settings with only the exception of the number of grid points. The number of grid points in CLES and traditional LES methods are identical while the number of grid points in DNS is significantly higher to resolve all necessary length scales. The simulation parameters are reported in Table 1, where $M_\infty = U_\infty / c_\infty$ is the free stream Mach number with c_∞ being the sound speed at the far field, $Re_\infty = \rho_\infty U_\infty / \mu_\infty$ is the Reynolds number, $T_\infty = 288.15\,\mathrm{K}$ is the free stream temperature, and T_w is the temperature at the wall boundary. The transport equations are discretized using a Cartesian grid of $N_x \times N_y \times N_z$ with uniform distribution in the streamwise and spanwise directions and hyperbolic tangent distribution in the wall-normal direction in a rectangular computational domain of $L_x \times L_y \times L_z = 4\pi \times 2.0 \times 4\pi/3$. Δx^+, Δy_w^+ and Δz^+ are the first grid

Table 1 Summary of computational parameters. The computational domains L_x, L_y and L_z are non-dimensionalized by channel half-height δ

Cases	M_∞	Re_∞	T_w/T_∞	Re_τ	$N_x \times N_y \times N_z$	Δx^+	Δy_w^+	Δz^+
C1-DNS	1.5	3000	1.0	222	400 × 210 × 320	7	0.3	3
C1-CLES	1.5	3000	1.0	223	64 × 65 × 64	44	1	15
C1-LES	1.5	3000	1.0	211	64 × 65 × 64	41	1	14
C2-DNS	2.0	3500	1.0	281	400 × 210 × 320	8.8	0.4	3.7
C2-CLES	2.0	3500	1.0	278	64 × 65 × 64	55	1.4	18
C2-LES	2.0	3500	1.0	263	64 × 65 × 64	52	1.3	17
C3-DNS	3.0	4880	1.0	462	400 × 210 × 320	14	0.7	6
C3-CLES	3.0	4880	1.0	461	64 × 65 × 64	90	2.2	30
C3-LES	3.0	4880	1.0	433	64 × 65 × 64	85	2.1	28

cell length in streamwise, wall-normal and spanwise directions, respectively, and they are normalized by the viscous length scale δ_v.

Periodic boundary conditions are applied to streamwise and spanwise directions. The non-slip boundary and isothermal conditions are set at the walls in the transverse direction. The convection terms are discretized by a seventh-order upwind scheme with the Steger-Warming flux splitting [42], and the viscous terms are approximated by an eighth-order central difference scheme. A third-order total variation diminishing type of Runge-Kutta method is applied for time advancing [43]. The flow is driven by a uniform body force, which is time-dependent and maintains a constant mass flux [44]. Laminar flow with random disturbance is used as the initial condition for the CLES and LES methods. In contrary to the CLES and LES methods, the statistically steady state solution from CLES is subsequently interpolated onto the DNS grid points to be used as an initial condition for the DNS method.

3 Results

3.1 Intermittency factor and transition process prediction

To evaluate the grid effect of the CLES method, we perform two more simulations with different grid resolutions for the C2-CLES case at $M_\infty = 2.0$ and $Re_\infty = 3500$. The grid settings of the coarser and the finer are $N_x \times N_y \times N_z = 48 \times 49 \times 48$ and $96 \times 97 \times 96$ respectively. As shown in Fig. 1, the evolution of Re_τ with time is identical for the C2-CLES case and the case with finer mesh configuration in the laminar and transition stage. While the Re_τ from the case with coarser mesh is a little bit larger than results from the other two CLES cases throughout the flow stage, which may be caused by higher dissipation of the coarser mesh. Furthermore, the Re_τ for C2-CLES and the case with finer mesh are almost the same in the fully developed turbulent stage. Therefore, the grid resolution of C2-CLES is enough for the CLES method and it is adopted in the following analysis.

Figure 2 shows the evolution of the intermittency factor γ from the three CLES cases, where it is equal to 0 in the laminar state and progresses towards unity in the turbulent state, indicating the intermittency factor to agree well with the transition process for all cases. It is worth noting that γ may be slightly larger or slightly smaller than 1 for different cases, and subsequent analysis shows that this has little effect on

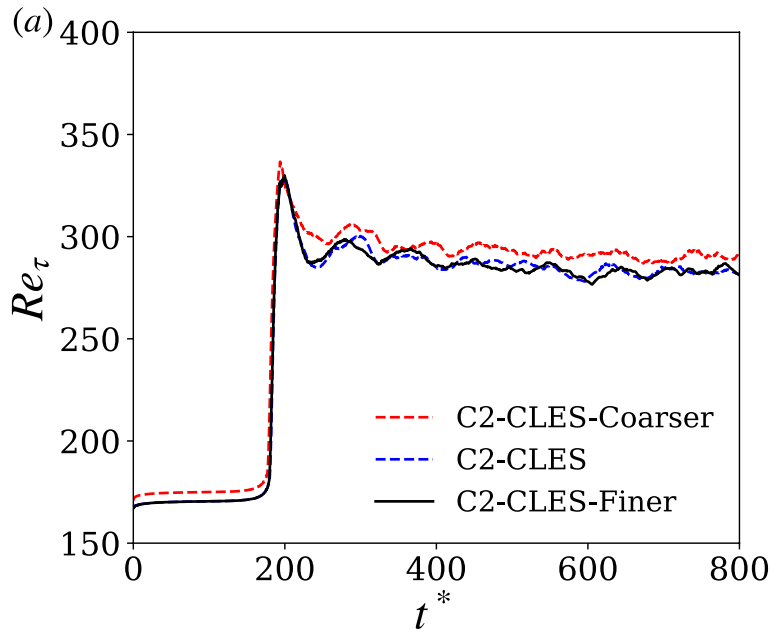

Fig. 1 Temporal evolution of the Re_τ from the C2-CLES case with different grid resolutions. t is normalized as: $t^* = tU_b/\delta$

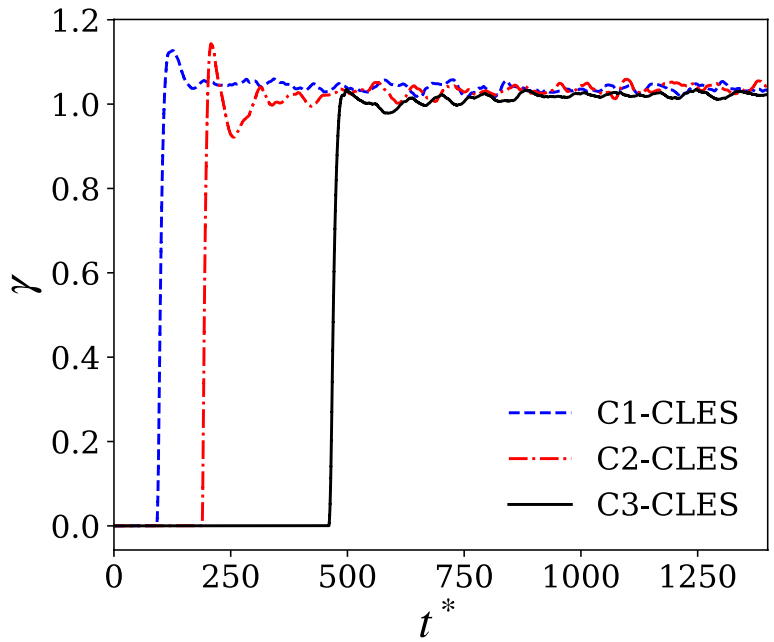

Fig. 2 Temporal evolution of the intermittency factor γ for C1-CLES, C2-CLES, and C3-CLES. t is normalized as: $t^* = tU_b/\delta$

the flow, which is also reported in Zhao et al.[31]. The Friction Reynolds numbers ($Re_\tau = \delta/\delta_v$) computed from the three different methods (LES, CLES, and DNS) of three cases are shown in Fig. 3. In the laminar stage, the predicted Re_τ from CLES and LES methods are slightly higher than the DNS results (eg. $t^* < 50$ for the $M_\infty = 1.5$).

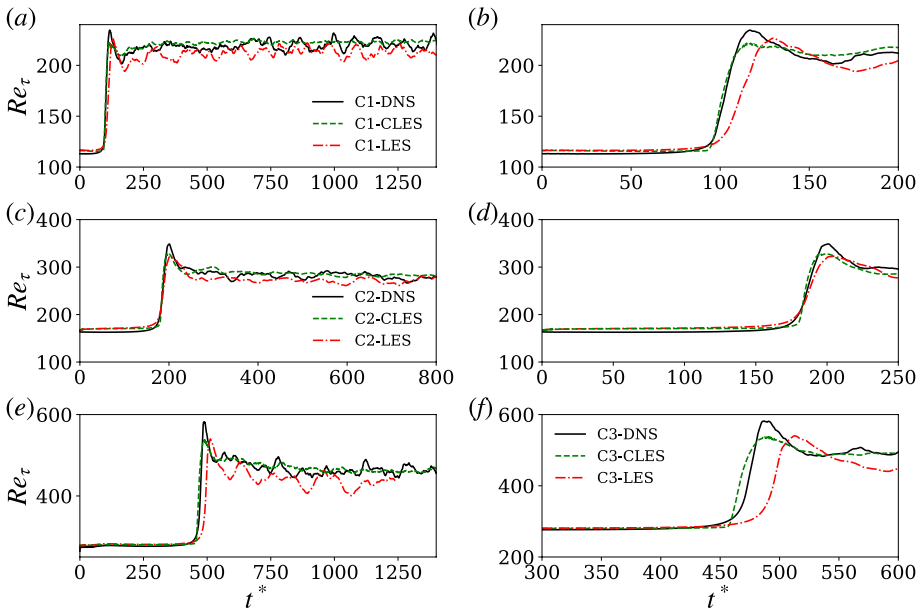

Fig. 3 Temporal evolution of Re_τ obtained from DNS, CLES, and LES methods for all three cases **a**, **b** C1, **c**, **d** C2, **e**, **f** C3

The transition from laminar to turbulent is found to occur at $t^* \approx 100$ for the C1 case with DNS and CLES is able to capture the transition period accurately (see Fig. 3(b)). However, the LES predicted a much later onset of the transition for the case of $M_\infty = 1.5$. While both LES and CLES methods can capture the rapid rise of Re_τ right after the transition to its peak, the CLES method has better agreement with the DNS results for all three cases. This is further reflected in the time-averaged values of Re_τ obtained from DNS, LES, and CLES (see Table 1), where the value predicted by CLES is in much closer agreement with the DNS result for all cases. It is worth mentioning here that the reported time-averaged value of Re_τ is computed after the flow becomes fully developed turbulence. It should also be noted that both CLES and LES underestimated the peak value of Re_τ at the late transition stage obtained from DNS data for all cases.

As shown in Section 2.2, the total Reynolds shear stress τ_{ij}^{RANS} for CLES and LES is the sum of the mean SGS stress $\left\langle \tau_{ij}^{LES} \right\rangle$ and the resolved Reynolds shear stress $-\left\langle \rho \tilde{u}_i'' \tilde{u}_j'' \right\rangle$, while the total Reynolds shear stress is expressed as $-\left\langle \rho u_i'' u_j'' \right\rangle$ in DNS. Reynolds stresses from different methods of the C2 case in the laminar and transition stages are shown in Fig. 4. In the laminar period of $t^* = 120$, both CLES and LES methods show great agreement in the near wall and channel center regions, and the CLES result also matches well to the DNS result in the area of $0.3 < y_w < 0.5$ while LES is worse than CLES. In the transition stage of $t^* = 180$, 200, and 220, both CLES and LES methods can only match the Reynolds stress in the region of $y_w < 0.15$ and show a significant discrepancy with the DNS result in the far from wall region. To sum up, CLES shows better performance than the traditional LES method near the wall, which is induced by the effect of the constrained model prescribed in the inner region of the computational domain [27].

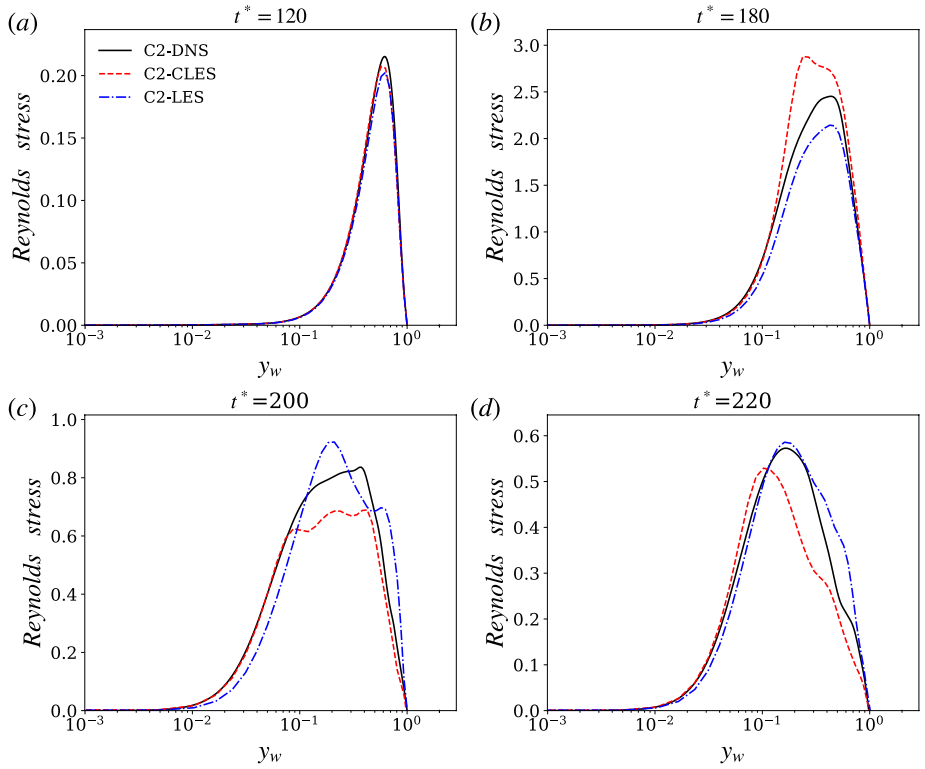

Fig. 4 Reynolds stresses in the laminar and transition stages of case C2. **a** $t^* = 120$; **b** $t^* = 180$; **c** $t^* = 200$; **d** $t^* = 220$

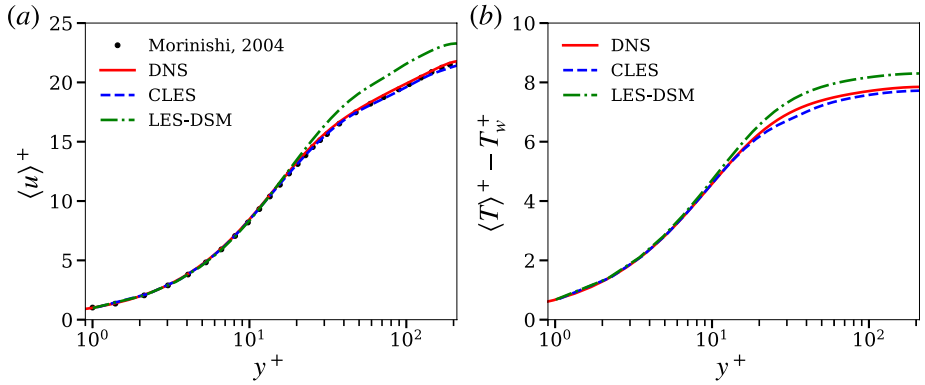

Fig. 5 Comparison of the **a** normalized mean streamwise velocity profiles $\langle u \rangle^+ = \langle u \rangle / u_\tau$ and **b** normalized temperature vs. normalized $y^+ = y/\delta_v$ obtained from present and previous studies

3.2 Statistics of fully developed turbulence

The normalized mean streamwise velocity profiles for fully developed turbulent state of case C1 obtained from DNS, CLES and LES are compared to Morinishi [45] in Fig. 5(a). The LES method overestimated the mean velocity profile at large y^+ values, while the CLES method agrees extremely well with the results from the present DNS and also previously obtained DNS by Morinishi et al. [45]. In addition, the normalized temperature $\langle u \rangle^+ - T_w^+$, where $T_\tau = -\langle q_w \rangle / \left(\langle \rho_w \rangle C_p u_\tau \right)$, obtained from present DNS, CLES, and

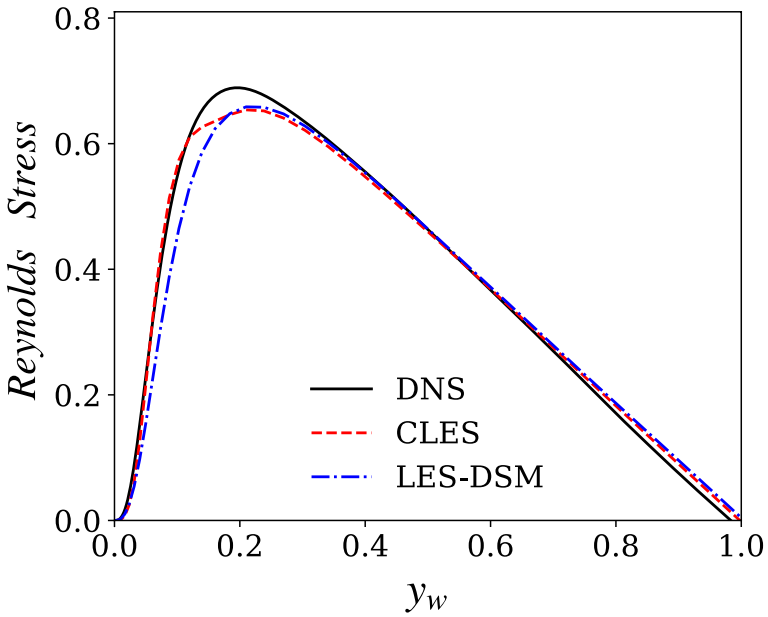

Fig. 6 The normalized total Reynolds stress vs. the normalized distance to the wall with the half height of the channel δ

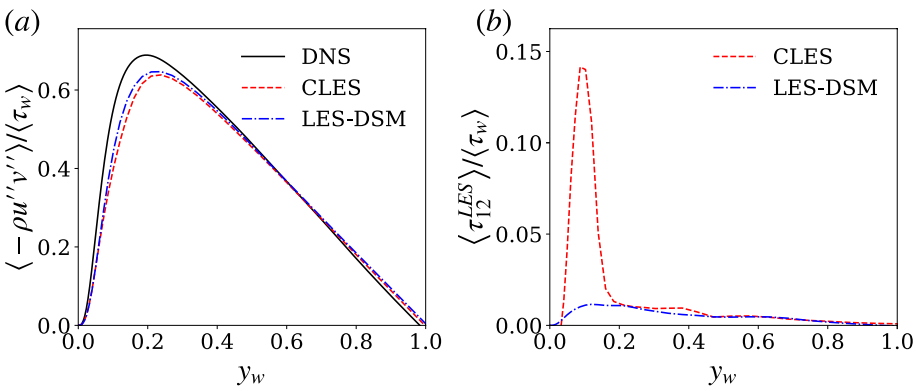

Fig. 7 The components of the normalized total Reynolds stress $\langle \tau_{12}^{RANS} \rangle / \langle \tau_w \rangle$ vs. the distance to the wall y_w: **a** the resolved Reynolds stress $-\langle \rho u'' v'' \rangle / \langle \tau_w \rangle$ and **b** the average of modeled SGS stress $\langle \tau_{12}^{LES} \rangle / \langle \tau_w \rangle$

LES are shown in Fig. 5(b). Similar to the results of mean streamwise velocity profile, the temperature distribution predicted by CLES is almost identical to the DNS results, but LES results deviate from DNS results at large y^+ ($y^+ > 10$).

Figure 6 shows the comparison of the Reynolds stress computed from DNS, LES, and CLES at $Re_\infty = 3000$ and $M_\infty = 1.5$. It is found that the peak value of the total Reynolds stress is within the viscous wall region ($y^+ < 50$), indicating the region with the most vigorous turbulent activity [46] and momentum exchange. In addition, the total Reynolds stress obtained from CLES agrees extremely well with the DNS data, except for the region near the interface. Nevertheless, the results obtained in CLES are far more superior than the traditional LES method in the near-wall constrained region.

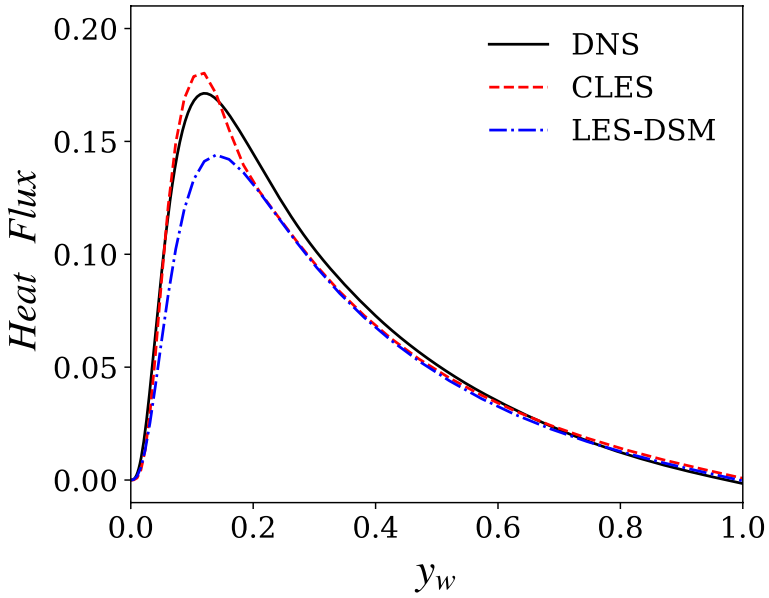

Fig. 8 The normalized total turbulent heat flux $\langle q_2^{RANS} \rangle / \langle q_w \rangle$ vs. the distance to the wall y_w

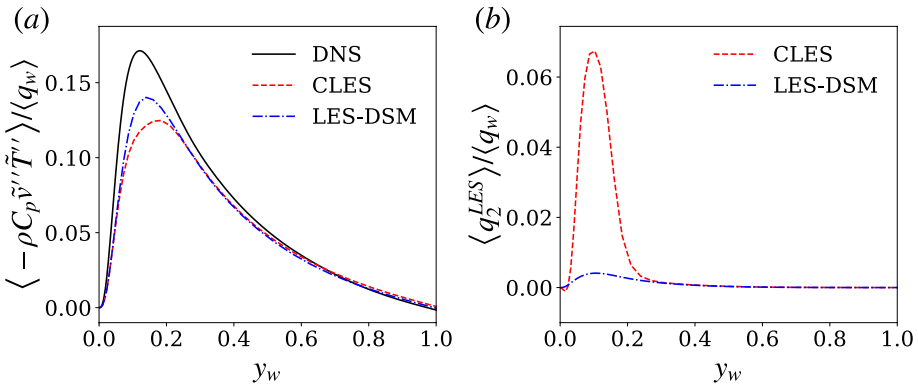

Fig. 9 The components of the normalized total Reynolds stress $\langle q_2^{RANS} \rangle / \langle q_w \rangle$ vary with the distance to the wall y_w: **a** the resolved Reynolds stress $-\langle \rho C_p v'' T'' \rangle / \langle q_w \rangle$ and **b** the average of modeled SGS stress $\langle q_{12}^{LES} \rangle / \langle q_w \rangle$

The components of the normalized total Reynolds stress from CLES and LES ($-\langle \rho \tilde{u}'' \tilde{v}'' \rangle / \langle \tau_w \rangle$) and DNS ($-\langle \rho u'' v'' \rangle / \langle \tau_w \rangle$) are shown in Fig. 7(a). The Reynolds stresses derived from CLES and LES are almost identical, but they deviate significantly from the DNS results in the viscous wall region. This is due to the lack of small-scale fluctuations in LES and CLES, where the introduction of the SGS stress models could improve the Reynolds stress predictions. As shown in Fig. 7(b), the mean modeled SGS stress is significantly different in the near-wall region due to the prescribed RANS model within the CLES framework. The value of the normalized modeled Reynolds stress grows to its peak rapidly in the buffer layer along the wall normal direction in the CLES method, yielding an order of magnitude larger than the DSM results. The value of $\langle \tau_{12}^{LES} \rangle$ decreases rapidly to 0 near the edge of the buffer layer and outer layer as expected.

Similarly to the total Reynolds stress τ_{ij}^{RANS}, the total turbulent heat flux is defined as the sum of the mean modeled SGS heat flux $\langle q_i^{LES} \rangle$ and the resolved turbulent heat flux $\left\langle \rho C_p \tilde{u}_i'' \tilde{T}'' \right\rangle$, and the modeled and the resolved heat flux are compared in Fig. 8. The turbulent heat flux reaches its peak in the buffer layer, indicating that the turbulent energy exchange in this region is energetic. The CLES method has an overall better agreement to the DNS result than the LES method, but some noticeable deviations from the DNS result can be observed near the interface of constrained and non-constrained regions.

Figure 9 shows the components of the total turbulent heat flux obtained using the CLES and DSM methods with the DNS results. The turbulent heat flux of DNS is expressed as $\langle \rho C_p u_i'' T'' \rangle$, which is significantly larger than the $\left\langle \rho C_p \tilde{u}_i'' \tilde{T}'' \right\rangle$ of CLES and DSM in the buffer layer. This further indicates that the coarse mesh filtered out many small scale fluctuations of the temperature field. In addition, the results obtained from the CLES and LES methods are consistent through the inner and outer layers, except for regions near the interface. The CLES modeled SGS heat flux is significantly larger than the DSM method in the inner region because of the effect of the constrained heat flux model as shown in Fig. 9(b).

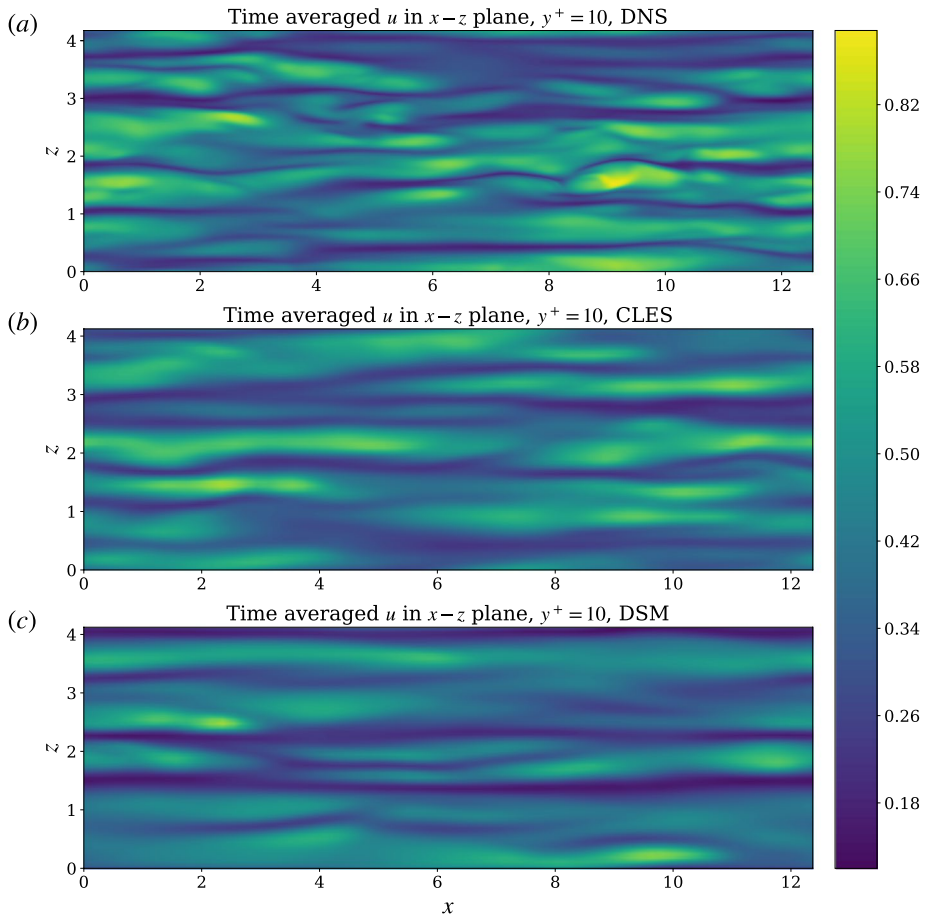

Fig. 10 The time averaged velocity field of u in $x-z$ plane at $y^+ = 10$ from DNS, CLES and DSM

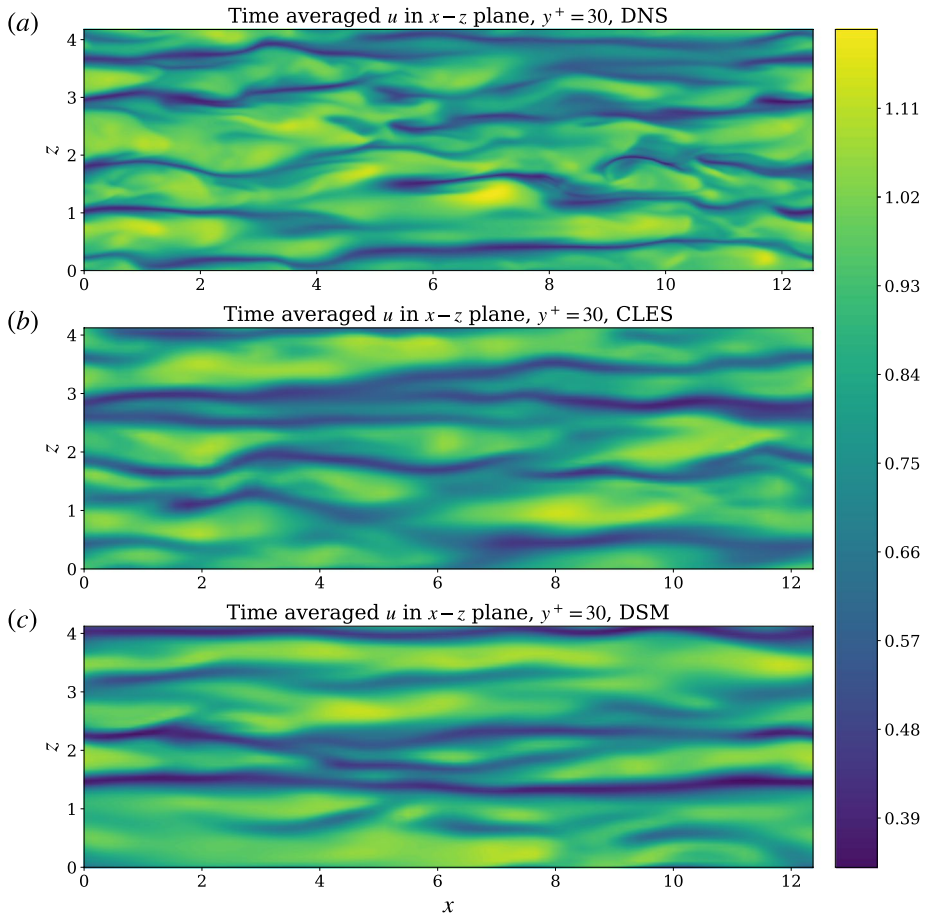

Fig. 11 The time averaged velocity field of u in $x-z$ plane at $y^+ = 30$ from DNS, CLES and DSM

The time averaged flow fields of streamwise velocity u at fully developed state in $x-z$ (x and z are normalized by the half height of the channel δ) plane at $y^+ = 10$ and $y^+ = 30$ from DNS, CLES, and LES are shown in Figs. 10 and 11, respectively. As shown in Fig. 10, the low speed streaks distribute uniformly in the DNS results, with the CLES results to be in better agreement to the DNS results than the LES results. In addition, the low speed streaks of DNS feature a thinner width and more meandering paths along the streamwise direction than the CLES and LES results, and this is mainly due to the lower grid resolution used in the CLES and LES methods. Nevertheless, the CLES performs much better in predicting the width and path of low speed streaks when compared to LES even at an identical grid resolution. Figure 11 exhibits similar characteristics to Fig. 10, but the velocity is higher in $y^+ = 30$ than $y^+ = 10$, suggesting the CLES to be more accurate in predicting the time averaged flow field.

4 Conclusion

In this paper, an intermittency factor based on the shape factor is introduced to improve the existing CLES method for compressible channel flows involving the temporal laminar-turbulent transition period. The proposed method is critically evaluated by comparing its performance on simulating channel flows at $M_\infty = 1.5$ and $Re_\infty = 3000$,

$M_\infty = 2.0$ and $Re_\infty = 3500$, and $M_\infty = 3.0$ and $Re_\infty = 4880$ with the widely used LES-DSM model and the DNS method. The time history of the Reynolds friction demonstrated that the CLES with intermittency factor could better capture the transition onset and the transition process than the traditional LES with DSM model. The Reynolds stresses during the transition show that both the LES with DSM and the improved CLES methods match well with the DNS result in the near wall region.

The Reynolds stresses and turbulent heat flux from CLES are further investigated and compared with DNS and LES methods, where the CLES method performs better than the traditional LES method in the inner region. Unfortunately, both CLES and LES methods failed to capture accurately the maximum Reynolds stress and turbulent heat flux near the buffer layer. However, the mean streamwise velocity and the mean temperature profiles obtained from CLES are in excellent agreement with the DNS result, while the LES method overestimated the streamwise velocity profiles in the log-law region and the temperature profiles at large y^+ ($y^+ > 10$).

All in all, the current CLES model coupled with the intermittency factor is capable of predicting accurately the transition process and onset in compressible channel flows. Most importantly, the proposed method maintained the original characteristics of CLES in terms of accurate predictions of the statistical properties of fully developed turbulence. Therefore, CLES shows great potential in simulating transitional flows, but more studies are warranted to develop better intermittency factor to accurately capture the physics near the interface, as well as in the spatial laminar-turbulent transition.

Acknowledgements
The authors would like to thank Prof. XinLiang Li for the open-source program OpenCFD and Prof. Yaomin Zhao for many helpful discussions on this work. We also would like to thank the Center for Computational Science and Engineering of Southern University of Science and Technology for supporting this project.

Authors' contributions
All authors read and approved the final manuscript.

Funding
This work was supported by the National Numerical Windtunnel project.

Availability of data and materials
The data that support the findings of this study are available from the corresponding author upon reasonable request.

Declarations

Competing interests
The authors declare that they have no competing interests.

Received: 6 October 2022 Accepted: 26 February 2023
Published online: 03 April 2023

References

1. Zhong X, Wang X (2012) Direct numerical simulation on the receptivity, instability, and transition of hypersonic boundary layers. Ann Rev Fluid Mech 44(1):527–561
2. Li F, Xie SF, Bi ZX, Gong J, Chen X, Ji F et al (2014) Experimental study of several on aerodynamic problems on hypersonic vehicles. Mod Def Technol 42(5):1–7
3. Fu S, Wang L (2013) RANS modeling of high-speed aerodynamic flow transition with consideration of stability theory. Prog Aerosp Sci 58:36–59
4. Orszag SA, Kells LC (1980) Transition to turbulence in plane Poiseuille and plane Couette flow. J Fluid Mech 96(1):159–205
5. Sayadi T, Hamman CW, Moin P (2013) Direct numerical simulation of complete H-type and K-type transitions with implications for the dynamics of turbulent boundary layers. J Fluid Mech 724:480–509
6. Zhao Y, Yang Y, Chen S (2016) Vortex reconnection in the late transition in channel flow. J Fluid Mech 802:R4. https://doi.org/10.1017/jfm.2016.492

7. Ducros F, Comte P, Lesieur M (1996) Large-eddy simulation of transition to turbulence in a boundary layer developing spatially over a flat plate. J Fluid Mech 326:1–36. https://doi.org/10.1017/S0022112096008221
8. Sayadi T, Moin P (2010) A comparative study of subgrid scale models for the prediction of transition in turbulent boundary layers. Annual Research Briefs 2010, Center for Turbulence Research, Stanford University, p 237–247. https://www.researchgate.net/publication/252698427_A_Comparative_Study_of_Subgrid_Scale_Models_for_Prediction_of_Transition_in_Turbulent_Boundary_Layers
9. Smagorinsky J (1963) General circulation experiments with the primitive equations: I. the basic experiment. Mon Weather Rev 91(3):99–164
10. Erlebacher G, Hussaini MY, Speziale CG, Zang TA (1992) Toward the large-eddy simulation of compressible turbulent flows. J Fluid Mech 238:155–185
11. Ghosal S, Lund TS, Moin P, Akselvoll K (1995) A dynamic localization model for large-eddy simulation of turbulent flows. J Fluid Mech 286:229–255
12. Yu C, Hong R, Xiao Z, Chen S (2013) Subgrid-scale eddy viscosity model for helical turbulence. Phys Fluids 25(9):095101
13. Zhou H, Li X, Qi H, Yu C (2019) Subgrid-scale model for large-eddy simulation of transition and turbulence in compressible flows. Phys Fluids 31(12):125118
14. Piomelli U, Balaras E (2002) Wall-layer models for large-eddy simulations. Ann Rev Fluid Mech 34(1):349–374
15. Menter FR, Langtry RB, Likki SR, Suzen YB, Huang PG, Völker S (2004) Acorrelation-based transitionmodel using local variables—Part I: model formulation. J Turbomach 128:413–422
16. Langtry RB, Menter FR, Likki SR, Suzen YB, Huang PG, Völker S (2004) A correlation-based transitionmodel using local variables—Part II: Test cases and industrial applications. J Turbomach 128:423–434
17. Langtry RB, Menter FR (2009) Correlation-based transition modeling for unstructured parallelized computational fluid dynamics codes. AIAA J 47(12):2894–2906
18. Krause M, Behr M, Ballmann J (2008) Modeling of transition effects in hypersonic intake flows using acorrelation-based intermittency model. In: 15th AIAA international space planes and hypersonic systems andtechnologies conference, American Institute of Aeronautics and Astronautics, Dayton, 28 April–1 May 2008
19. Bensassi K, Lani A, Rambaud P (2012) Numerical investigations of local correlation-based transition model inhypersonic flows. In: 42nd AIAA fluid dynamics conference and exhibit, American Institute of Aeronautics and Astronautics, New Orleans, 25–28 June 2012
20. Zhang YF, Lei J, Zhang YR, Mao ML, Chen JQ (2015) Calibration of transition model for hypersonic numerical simulation platform. Acta Aerodyn Sin 33(1):42–47
21. Zhang YF, He K, Zhang YR, Mao ML, Chen JQ (2016) Improvement and validation of Menter's transition model for hypersonic flow simulation. J Astronaut 37(4):397–402
22. Spalart PR (2000) Strategies for turbulence modelling and simulations. Int J Heat Fluid Flow 21(3):252–263
23. Spalart PR, Deck S, Shur ML, Squires KD, Strelets MK, Travin A (2006) A new version of detached-eddy simulation, resistant to ambiguous grid densities. Theor Comput Fluid Dyn 20(3):181–195
24. Deck S (2012) Recent improvements in the Zonal Detached Eddy Simulation (ZDES) formulation. Theor Comput Fluid Dyn 26(6):523–550
25. Spalart PR (2009) Detached-eddy simulation. Ann Rev Fluid Mech 41:181–202
26. Shur ML, Spalart PR, Strelets MK, Travin AK (2008) A hybrid RANS-LES approach with delayed-DES and wall-modelled LES capabilities. Int J Heat Fluid Flow 29(6):1638–1649
27. Chen S, Xia Z, Pei S, Wang J, Yang Y, Xiao Z, Shi Y (2012) Reynolds-stress-constrained large-eddy simulation of wall-bounded turbulent flows. J Fluid Mech 703:1–28
28. Jiang Z, Xiao Z, Shi Y, Chen S (2013) Constrained large-eddy simulation of wall-bounded compressible turbulent flows. Phys Fluids 25(10):106102
29. Zhang W, Wan M, Xia Z, Wang J, Lu X, Chen S (2021) Constrained large-eddy simulation of turbulent flow over inhomogeneous rough surfaces. Theor Appl Mech Lett 11(1):100229. https://doi.org/10.1016/j.taml.2021.100229
30. Zhang W, Wan M, Xia Z, Wang J, Lu X, Chen S (2021) Constrained large-eddy simulation of turbulent flow over rough walls. Phys Rev Fluids 6:044602. https://doi.org/10.1103/PhysRevFluids.6.044602
31. Zhao Y, Xia Z, Shi Y, Xiao Z, Chen S (2014) Constrained large-eddy simulation of laminar-turbulent transition in channel flow. Phys Fluids 26(9):095103
32. Wang X, Xiao Z (2022) Transition-based constrained large-eddy simulation method with application to an ultrahigh-lift low-pressure turbine cascade flow. J Fluid Mech 941:A22
33. Pino Martín M, Piomelli U, Candler GV (2000) Subgrid-scale models for compressible large-eddy simulations. Theor Comput Fluid Dyn 13(5):361–376
34. Yoshizawa A (1986) Statistical theory for compressible turbulent shear flows, with the application to subgrid modeling. Phys Fluids 29(7):2152–2164
35. Moin P, Squires K, Cabot W, Lee S (1991) A dynamic subgrid-scale model for compressible turbulence and scalar transport. Phys Fluids A Fluid Dyn 3(11):2746–2757
36. Wilcox DC (1997) Turbulence modeling for CFD, 2nd edn. DCW Industries, La Canada
37. Baldwin B, Lomax H (1978) Thin-layer approximation and algebraic model for separated turbulentflows. In: 16th aerospace sciences meeting, American Institute of Aeronautics and Astronautics, Huntsville, 16–18 January 1978
38. Menter FR, Rumsey CL (1994) Assessment of two-equation turbulence models for transonic flows. In: Fluid dynamics conference, American Institute of Aeronautics and Astronautics, Colorado Springs, 20–23 June 1994
39. Simon F, Deck S, Guillen P, Sagaut P, Merlen A (2007) Numerical simulation of the compressible mixing layer past an axisymmetric trailing edge. J Fluid Mech 591:215–253
40. Piomelli U, Zang TA, Speziale CG, Hussaini MY (1990) On the large-eddy simulation of transitional wall-bounded flows. Phys Fluids A Fluid Dyn 2(2):257–265
41. Kundu PK, Cohen IM, Dowling DR (2015) Fluid mechanics, 6th edn. Academic press, San Diego
42. Jiang GS, Shu CW (1996) Efficient implementation of weighted ENO schemes. J Comput Phys 126(1):202–228

43. Shu CW, Osher S (1988) Efficient implementation of essentially non-oscillatory shock-capturing schemes. J Comput Phys 77(2):439–471
44. Lenormand E, Sagaut P, Ta Phuoc L (2000) Large eddy simulation of subsonic and supersonic channel flow at moderate Reynolds number. Int J Numer Methods Fluids 32(4):369–406
45. Morinishi Y, Tamano S, Nakabayashi K (2004) Direct numerical simulation of compressible turbulent channel flow between adiabatic and isothermal walls. J Fluid Mech 502:273–308. https://doi.org/10.1017/S0022112003007705
46. Pope SB (2000) Turbulent Flows. Cambridge University Press, Cambridge. https://doi.org/10.1017/CBO9780511840531

Publisher's Note